

The Optimization of Curcumin-Capped Gold Nanoparticle Synthesis for FLuc-mRNA Delivery to Cervical Cancer Cells *in vitro*

Janeen Venkatas¹ , Aliscia Daniels¹ , Moganavelli Singh^{1,*} 

¹ Nano-Gene and Drug Delivery Group, Discipline of Biochemistry, University of KwaZulu-Natal, Private Bag X54001, Durban, South Africa

* Correspondence: singhm1@ukzn.ac.za (M.S.);

Scopus Author ID 3709591900

Received: 16.09.2022; Accepted: 30.10.2022; Published: 6.01.2023

Abstract: Gold nanoparticles (AuNPs) have attracted interest owing to their widespread biological and technological applications. AuNPs can enhance the targeted delivery of photosensitive and therapeutic material to tumor cells. Curcumin, a bioactive secondary metabolite isolated from *Curcuma longa*, exhibits favorable pharmacological properties, enabling synergistic activity with the therapeutic cargo. This study aimed to determine the optimal concentration of curcumin needed to produce curcumin-capped AuNPs that would best deliver FLuc-mRNA to cervical cancer cells *in vitro*. AuNPs were reduced using varying concentrations of curcumin, functionalized with poly-L-lysine (PLL) for mRNA binding, and stabilized using polyethylene glycol. Nanoparticle characterization using UV-vis and Fourier-transform infrared spectroscopy confirmed the synthesis and functionalization of the AuNPs. Nanoparticle tracking analysis (NTA) and transmission electron microscopy (TEM) confirmed the presence of spherical AuNPs of a favorable size for gene therapy. Adequate compaction and nuclease protection of the mRNA by the AUNPs was evident using binding and nuclease protection assays. Significant transgene expression was observed using the luciferase reporter gene assay, while the 3-(4,5-dimethylthiazol-2-yl)-2,5-diphenyltetrazolium bromide (MTT) assay revealed high cell viability (77%) *in vitro*. Overall, 1 mM curcumin-capped AuNPs demonstrated the most favorable attributes of a gene delivery vehicle to be considered for future studies.

Keywords: gold nanoparticles; cancer; curcumin; mRNA; cytotoxicity; gene expression.

© 2023 by the authors. This article is an open-access article distributed under the terms and conditions of the Creative Commons Attribution (CC BY) license (<https://creativecommons.org/licenses/by/4.0/>).

1. Introduction

Cancer is the second leading cause of death worldwide, with an annual incidence and mortality rate of 18.1 million and 9.6 million, respectively. Cervical cancer (CC) is the fourth most common cancer in women globally, with an estimated 570,000 novel cases and 311,000 deaths annually [1]. Despite the many advances in cancer therapy, the disease's incidence and mortality have not declined in the past 30 years [2-3]. Recent advances in nanomedicine have created a niche for the development of anticancer strategies which target the tumor microenvironment (TME) to inhibit tumor development, progression, and metastasis without causing severe side effects [4].

In addition to physical and chemical nanoparticle (NP) synthesis, green synthesis using bioactive plant compounds has shown great potential in reducing metal ion precursors to NPs. Several anticancer agents with various modes of action have been extracted from plant sources,

including *Croton sparsiflorus*, *Ledebouria revoluta*, *Nigella sativa*, and *Curcuma longa* [3,5-7]. Among these biological extracts, curcumin, the principal curcuminoid obtained from the rhizomes of *C. longa*, was first isolated in 1870. Curcumin has received immense attention in the past two decades due to its biological properties such as antioxidant, hypotensive, anti-inflammatory, anticoagulant, antifertility, antiulcer, antimicrobial, antivenom, antifibrotic, antimutagenic, antidiabetic, anticarcinogenic and most importantly, anticancer activities [8]. Curcumin induces apoptosis while inhibiting the proliferation and invasion of tumors by suppressing various cellular signaling pathways [9].

However, despite the anticancer properties of curcumin seen in thyroid, prostate, lung, liver, myeloma, pancreatic, melanoma, colorectal breast, and cervical cancer, the use of this multi-functional biomolecule is limited. This is due to curcumin's low cellular uptake and poor aqueous solubility, resulting in its poor chemical stability and oral bioavailability [10-13]. Decreasing the size of the curcumin improves its solubility and, as a result, bioavailability, which is the aim of most studies to date. This has led to the formulation of organic or inorganic NPs enveloped by curcumin. Curcumin-capped NPs reduce the amount of the therapeutic component needed, which improves therapeutic indices while reducing toxicity [14, 15].

Gold NPs (AuNPs) serve as potential therapeutic gene delivery vehicles due to their favourable properties such as ease of manufacturing, tunable stability, resilience, low cytotoxicity, biodegradability, biocompatibility, protection of the gene from systemic degradation, and amenability to surface modification [16,17]. Rejinold *et al.* demonstrated targeted delivery of therapeutic agents and enhanced apoptosis in colon tumor cells using curcumin-reduced and capped chitosan-AuNPs [18]. Similarly, curcumin-capped AuNPs effectively induced apoptosis in prostate and renal cancer cells [13,19]. Curcumin's antioxidant property facilitates the reduction of the gold salt to produce AuNPs [12]. Further stabilization of the AuNPs can be obtained by functionalization with polymers such as poly-L-lysine (PLL) and polyethylene glycol (PEG) [20,21]. PLL is a cationic polymer that electrostatically binds to the negatively charged phosphate backbone of the nucleic acid [22]. The use of PEG (PEGylation) enhances the therapeutic effect of the gene by reducing rapid renal clearance and prolonging *in vivo* circulation time by preventing opsonization and removal by the reticuloendothelial system (RES) [21,23]. This study examined varying concentrations of curcumin to synthesize AuNPs, to optimize the safety and delivery of *FLuc*-mRNA to human cervical carcinoma (HeLa) cells *in vitro*.

2. Materials and Methods

2.1. Materials.

Sodium dodecyl sulfate (SDS, Mw: 288.37 g/mol), ethidium bromide (EB) (10 mg/ml) solution, ethylene diamine tetra-acetic acid disodium salt (Mw: 372.24 g/mol, EDTA), phosphate-buffered saline tablets (PBS), tris (hydroxymethyl) aminomethane (Tris base, Mw: 121.14 g/mol), and trisodium citrate dehydrate (Mw: 294.20 g/mol) 2-[4-(2-hydroxyethyl) piperazin-1-yl] ethane sulphonic acid (HEPES), 3-(4,5-dimethylthiazol-2-yl)-2,5-diphenyltetrazolium bromide (MTT), and bromophenol blue (Mw: 669.96 g/mol), were obtained from Merck (Darmstadt, Germany). RNase-free water (1 U/ μ l, with $MnCl_2$) and agarose were supplied by Thermo Fischer Scientific Inc. (Waltham, Massachusetts, USA). Gold (III) chloride trihydrate (Mw: 393.83 g/mol, $HAuCl_4 \cdot 3H_2O$), poly-L-lysine hydrobromide (Mw: 1000-5000, PLL), polyethylene glycol 2000 (PEG), bicinchoninic acid (BCA) kit,

curcumin (Mw: 368,38 g/mol), and dialysis tubing (MWCO 12 kDa), were purchased from Sigma-Aldrich (St. Louis, MO, USA). *FLuc*-mRNA was produced by TriLink Bio Technologies, Inc (San Diego, CA, USA). The human embryonic kidney (HEK293) and cervical carcinoma (HeLa) cell lines were sourced from the American Type Culture Collection (ATCC) (Manassas, VA, USA) and were used after the second passage. Sterile cell culture plasticware was procured from Nest Biotechnologies (Wuxi, China), and the Eagles minimum essential medium (EMEM), trypsin-versene, antibiotics (penicillin (5000 U/ml)/streptomycin (5000 g/ml), were supplied by Lonza BioWhittaker (Walkersville, MD, USA). Gamma-irradiated fetal bovine serum (FBS) was obtained from Cytiva Europe GmbH, Vienna, Austria. The Promega Corporation (Madison, WI, USA) provided the luciferase assay kit.

2.2. AuNP synthesis.

Four concentrations of curcumin, 0.25 mM, 0.5 mM, 0.75 mM, and 1 mM, were used to synthesize AuNPs from HAuCl_4 . Briefly, a curcumin stock was prepared in DMSO and diluted to the desired concentrations with 18 M Ω water, pH 9.3. The curcumin solution (1 mL) was added dropwise (5 min intervals) with stirring to 9 ml of HAuCl_4 (1 mM) at room temperature. The sample was stirred for 2 h and matured in an opaque tube for three days at room temperature. The sample was then pelleted at 10 000 rpm for 15 min to remove unreacted curcumin, and the pellet was resuspended in 18 M Ω water (Figure 1).

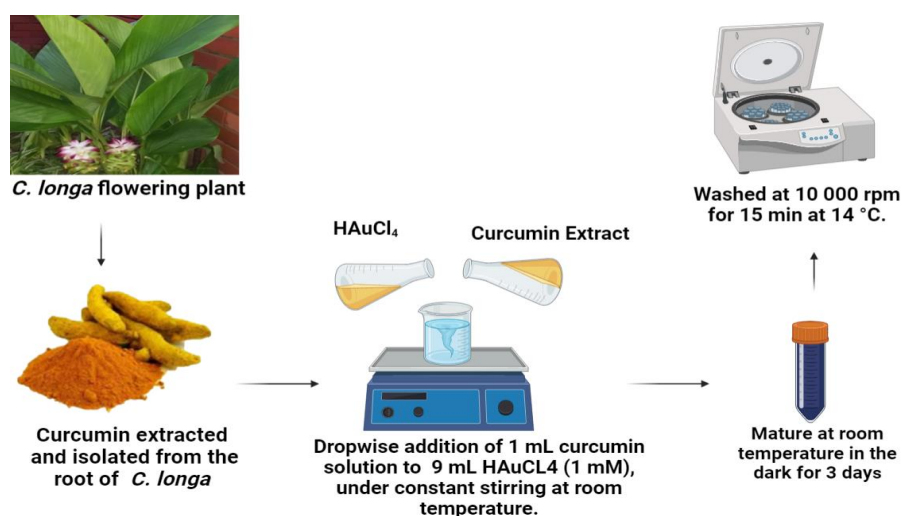


Figure 1. Curcumin-mediated gold nanoparticle synthesis.

2.3. Modification of AuNPs with PLL and PEG.

AuNP-PLL (1:1 ratio) was prepared by gradually adding the AuNP solution to a 1% PLL solution over 2 h, with constant stirring. The AuNP-PLL solution was dialyzed (MWCO 12 kDa) against 18 M Ω water for 2 h to remove any unbound PLL. To produce a 2% (w/w) AuNP-PLL-PEG, PEG2000 (1 mg/ml) was added dropwise (3 min intervals) to AuNP-PLL with stirring over 2 h [21]. Unbound PEG was removed by dialysis, and NPs were stored at 4°C.

2.4. *FLuc*-mRNA nanocomplex preparation.

To a constant amount of *FLuc*-mRNA (0.3 $\mu\text{g}/\mu\text{l}$), varying amounts of each functionalized AuNP were added to produce increasing weight ratios. This was incubated at

room temperature for 30 mins to allow for the formation of *FLuc*-mRNA:AuNP-PLL and *FLuc*-mRNA:AuNP-PLL-PEG nanocomplexes.

2.5. Characterization.

Initial confirmation for the formation of the AuNPs and functionalized AuNPs was obtained using UV-vis spectroscopy. Confirmation was based on changes in their surface plasmon resonance (SPR) within a 200-700 nm wavelength range using a JASCO-V-730-Biospectrometer (JASCO Corporation, Japan).

Transmission electron microscopy (TEM) using a Jeol T-1010 TEM (Tokyo, Japan) was used to assess the dry size and morphology of the NPs and nanocomplexes. For TEM, carbon-coated copper grids (400-mesh, Ted Pella Inc. Redding, CA, USA) were submerged in the respective samples and air-dried before viewing and capturing images using a Soft Imaging Systems MegaView III side-mounted 3-megapixel digital camera. The zeta potentials, hydrodynamic sizes, and polydispersity indices (PDI) of the diluted (1:100 in 18 MΩ H₂O) NPs and nanocomplexes (at optimally mRNA binding) were determined using nanoparticle tracking analysis (NTA) (Nanosight NS500, Malvern Instruments, Worcestershire, UK).

Fourier-transform infrared (FTIR) spectroscopy was conducted using a Perkin Elmer Spectrum 100 FTIR spectrometer in a 4000 - 400 cm⁻¹ wavelength range. The stability of NPs was further evaluated for nine months at room temperature by measuring a change in SPR and zeta potential.

2.6. Electrophoretic mobility shift assay.

The electrophoretic mobility shift or band shift assay [24] was utilized to determine the optimum, sub-optimum, and supra-optimum binding ratios (w/w) of the *FLuc*-mRNA to the functionalized AuNPs (AuNP-PLL and AuNP-PLL-PEG). Nanocomplexes were prepared (Section 2.4), with mRNA:NP (w/w) ratios ranging from 1:0 -1:1.4 (Table 1).

Table 1. Preparation of nanocomplexes for the band-shift and nuclease digestion assays.

Components		Ratios							
		1:0	1:0.2	1:0.4	1:0.6	1:0.8	1:1	1:1.2	1:1.4
mRNA	(μL)	1.00	1.00	1.00	1.00	1.00	1.00	1.00	1.00
	(μg/μl)	(0.30)	(0.30)	(0.30)	(0.30)	(0.30)	(0.30)	(0.30)	(0.30)
AuNP-PLL*	(μL)	0	0.60	1.20	1.80	2.40	3.00	3.60	4.20
	(μg/μl)	(0)	(0.06)	(0.12)	(0.18)	(0.24)	(0.30)	(0.36)	(0.42)
AuNP-PLL-PEG**	(μL)	0	0.59	1.18	1.76	2.35	2.94	3.53	4.11
	(μg/μl)	(0)	(0.06)	(0.12)	(0.18)	(0.24)	(0.30)	(0.36)	(0.42)

Functionalized NPs diluted to a concentration of *0.1001 μg/μL and **0.1021 μg/μL

The positive control used was naked *FLuc*-mRNA (0.3 μg/μl). Nanocomplexes containing 2 μl gel loading buffer (40% sucrose and 0.25% bromophenol blue) were added to their respective wells in an agarose gel (1%, w/v) containing 2 μl of a 10 mg/ml stock of ethidium bromide (EB). Electrophoresis was carried out for 30 min at 55 V in a Bio-Rad Mini-Sub® electrophoretic apparatus (Richmond, VA, USA). Gel images were viewed and captured using a Vacutec Syngene G-Box BioImaging system (Syngene, Cambridge, UK).

2.7. Ethidium bromide displacement assay.

The EB assay evaluated the extent to which the functionalized AuNPs could condense and compact the mRNA [24]. The baseline fluorescence (0%) was first set by measuring the

fluorescence of EB (2 μ l of a 100 μ g/mL stock) in 100 μ l of HBS in a 96-well FluorTrac flat-bottomed black plate (Greiner Bio-One, Frickenhausen, Germany) at an excitation wavelength of 520 nm and an emission wavelength of 610 nm in a GloMax®-Multi Detection System (Promega BioSystems, Sunnyvale, CA, USA). To this was added 1 μ l of mRNA (0.3 μ g/ μ l), and the observed fluorescence was set as 100%. Aliquots (1 μ l) of the respective functionalized AuNPs were added, and fluorescence was measured until a point of inflection or a plateau in readings was noted. The relative fluorescence (FR) was calculated as in equation 1 [25], where F_i is the fluorescence reading after NP addition, F_0 is the reading of EB with no mRNA, and F_{max} is the reading after mRNA addition.

$$FR (\%) = \frac{F_i - F_0}{F_{max} - F_0} \times 100 \quad (1)$$

2.8. mRNA protection assay.

The nuclease protection assay indicated the level of protection offered to the mRNA by the functionalized AuNPs against nucleases under normal physiological conditions [24]. Sub-optimum, optimum, and supra-optimum nanocomplex ratios (w/w) (Table 2) were assessed. Nanocomplexes were treated with FBS (10%, v/v) and incubated at 37 °C for 4 h. Nuclease activity was terminated using 10 mM of EDTA, and the mRNA was liberated from the NPs by adding 5% (w/v) SDS followed by incubation for 20 mins at 55 °C. Two controls were set up, a positive control (P) with mRNA only and negative control (N) with mRNA treated with FBS.

Table 2. Sub-optimum, optimum, and supra-optimum (w/w) nanocomplex ratios obtained from the band-shift assay.

Nanocomplexes	Sub-optimal	Optimal	Supra-optimal
PLL-AuNP ^{0.25}	1:1	1: 1.2	1:1.4
PEG-PLL-AuNP ^{0.25}	1:1	1: 1.2	1:1.4
PLL-AuNP ^{0.5}	1:1	1: 1.2	1:1.4
PEG-PLL-AuNP ^{0.5}	1:1.2	1: 1.4	1:1.6
PLL-AuNP ^{0.75}	1:1.2	1: 1.4	1:1.6
PEG-PLL-AuNP ^{0.75}	1:1.2	1: 1.4	1:1.6
PLL-AuNP ¹	1: 0.8	1: 1	1: 1.2
PEG-PLL-AuNP ¹	1: 0.8	1: 1	1: 1.2

2.9. MTT cell viability assay

The cytotoxicity of the nanocomplexes was examined in the HeLa and HEK293 cells using the MTT assay [25]. The cells were trypsinized and seeded into 96-well plates at a density of 3×10^5 cells per well and incubated for 24 h at 37 °C. The medium was then replenished with a complete medium (EMEM + 10% FBS + 1% antibiotics) containing the nanocomplexes at the optimum, sub-optimum, and supra-optimum ratios (in triplicate). Two controls were used, mRNA only and untreated cells (used as 100% cell survival). The treated cells were incubated at 37 °C for 48 h. The medium was thereafter replaced with MTT (10 μ L, 5 mg/mL in PBS) in 100 μ L EMEM and cells were incubated at 37 °C for 4 h. Subsequently, the medium was discarded, and DMSO (100 μ L) was added to dissolve the formazan crystals. The absorbance was measured at 570 nm in a Mindray MR-96A microplate reader (Vacutec, Hamburg, Germany), using DMSO as a blank.

2.10. Luciferase reporter gene assay.

Cells were seeded and treated as described in Section 2.9. Two controls, as in section 2.9, were employed. Following the 48 h incubation period at 37 °C, the medium was disregarded, and cells were washed twice with 100 µL PBS. Thereafter, 80 µL of cell lysis buffer was added to each well, followed by gentle shaking for approximately 15 mins. The cell suspensions were centrifuged for 5 s at 12 000 ×g. The supernatant (20 µL), together with 100 µL of the luciferase assay reagent in a white 96-well plate, was assessed for luminescence in a GloMax®-Multi Detection System (Promega BioSystems, Sunnyvale, CA, USA). The bicinchoninic acid (BCA) assay was used to determine the protein content of the cell lysates. This was used to normalize the luciferase activity, which was finally reported as relative light units (RLU) per mg of protein.

2.11. Statistical analysis.

All assays were carried out in triplicate, and the data were presented as means and standard deviation (SD). The multiple-group comparisons of the means were performed using a two-way analysis of variance (ANOVA). This was followed by Tukey's multiple comparisons post hoc test. All statistics were performed using a 95% CI and were considered significant, * $p < 0.05$ (significant), ** $p < 0.01$ (highly significant), and *** $p < 0.001$ (very highly significant).

3. Results and Discussion

3.1. Synthesis and characterization of AuNPs.

AuNPs have gained much attention due to their widespread biological and technological applications. Their facile synthesis via green chemistry has gained momentum [12,16,19]. This paper aimed to optimize the synthesis of spherical AuNPs using curcumin as the reducing and stabilizing agent. UV-vis spectroscopic studies are one of the essential tools used to confirm the formation of NPs. Under the UV region, gold NPs display a characteristic absorbance band due to the excitation mode of their surface plasmons [26]. AuNPs were successfully synthesized, capped with curcumin, and functionalized with PLL and PEG, as initially confirmed by the UV-vis spectroscopy in Figure 2. A single peak indicated the colloidal solution was free of by-products or contaminants [27, 28]. Nanostructured metallic particles have a free electron abundance which migrates through the conduction and valence band. This, together with the vibration within the gold metal in resonance with the light wave, is responsible for SPR [29]. The plasmon bands are broadened with an absorption tail at longer wavelengths, which may be due to the size distribution of the particles [26].

The curcumin-reduced and capped NPs produced a distinct peak at the maximum absorbance wavelength of ± 525 nm [21]. However, the aggregation of AuNPs during the reduction of its metal salt poses a significant challenge, enforcing the need for stabilization [30, 31]. Redshifts and broader peaks were observed for all the AuNP-PLL and AuNP-PLL-PEG, indicating successful attachment and functionalization of the PLL and PEG motifs to the AuNP.

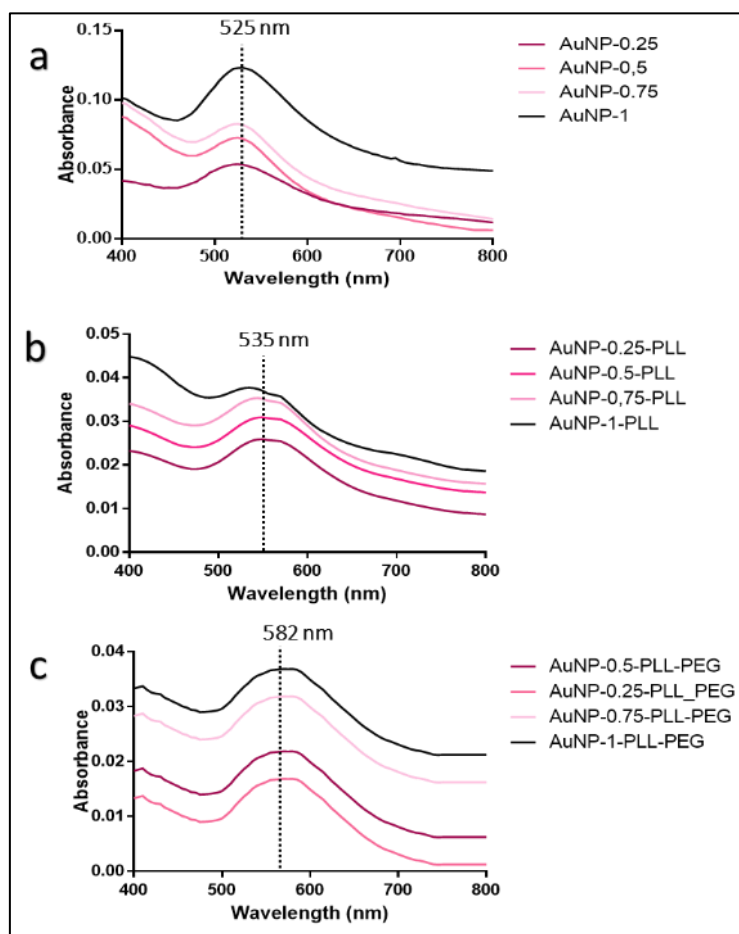


Figure 2. UV-vis spectra of (a) AuNP, (b) AuNP-PLL, and (c) AuNP-PLL-PEG synthesized with 0.25 mM, 0.5 mM, 0.75 mM, and 1 mM curcumin.

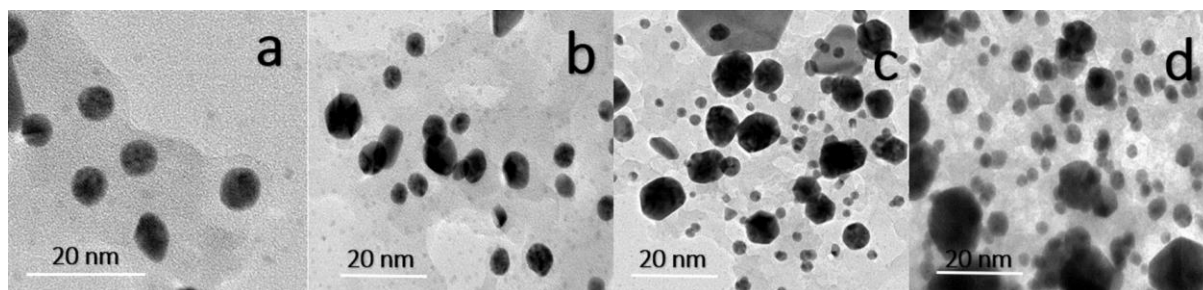
PLL and PEG polymers have proven to be effective stabilizers of gold NPs. PLL creates a positive charge around the AuNP, facilitating their binding to nucleic acids and their uptake by the cell [28, 22]. PEGylation using the non-immunogenic, biocompatible PEG prevents the immune recognition of the NPs and their opsonization by proteins. PEGylation further protects the therapeutic agents from immune recognition and prolongs their blood circulation time [32].

Successful functionalization was further confirmed by FTIR, TEM, and NTA [20,21]. FTIR analysis identified the functional groups involved in reducing and capping the AuNPs (Supplementary Figures S1-S3) [12]. The additional PLL and PEG peaks observed further indicated successful conjugation of the PLL and PEG moieties. The important peaks are summarized in Table 3. The asymmetric carboxylate stretching band at 1620-1640 cm^{-1} represented the successful synthesis of AuNPs. The distinct peak at 1525.11 cm^{-1} is the aromatic rings' stretching vibration, confirming the enolic-H's replacement on the curcumin by the AuNP. The carbonyl group of the enolic curcumin aids in reducing and capping the HAuCl_4 [33,34]. The broad peaks observed at 2930.18 cm^{-1} and 3236.45 cm^{-1} indicate stretching of the CH and an amide A group corresponding to the PLL conformation. This suggests the successful conjugation of the PLL [20,35]. Successful PEGylation of PLL-AuNPs was indicated by stretching of CH_2 (2915.93 cm^{-1}) and C-O-C (1037.58 cm^{-1}) of the PEG chains [21,36].

Table 3. FTIR spectra of chemically and biologically synthesized and functionalized AuNPs.

Supplementary Figures	Wavenumber (cm ⁻¹)	Functional groups
Figure S1	1620-1640	C=O stretching
Figure S2	3236.45	Amide A
	2930.18	C-H stretching
Figure S3	1037.58	C-O stretching
	2915.93	C-H stretching

TEM results further confirmed the successful synthesis and functionalization of the NPs as visualized by an increase in size following the addition of each polymer (Figure 3). TEM revealed well-distributed spherical and smooth NPs with little or no agglomeration. Studies have revealed that particle size is essential for the permeation and retention into the TME, influencing NP-mediated transfection by controlling NP adhesion and interaction with cells [37]. This study's nanometer-sized particles (< 150 nm) are ideal for gene therapy applications. TEM analysis revealed NP sizes between 10.58 and 11.86 nm, while the hydrodynamic sizes (NTA) were significantly larger due to the hydrodynamic shell formed within the colloidal solution and ranged from 70.0 to 153.9 nm (Table 4). The hydrodynamic sizes of the NPs increased upon the addition of each polymer. This increase was consistent with the redshift in the maximum wavelength observed under UV-vis spectroscopy. The TEM images illustrate a decrease in the size of the AuNPs with an increase in the concentration of curcumin. The size change could be due to the availability of more functional groups to stabilize the NPs [38,39]. However, variations of the shapes and sizes of the AuNP-PLL-PEG, as depicted by the TEM (Figure 4C), could be due to the different phytochemicals used in green chemistry [40]. It was observed that even plants grown in different geographical areas or harvested at different times could produce bioactive constituents that have slightly varied properties [41].

**Figure 3.** TEM images of 1 mM curcumin-capped AuNP and their functionalized AuNPs. (a) AuNP, (b) AuNP-PLL, (c) AuNP-PLL-PEG, and (d) AuNP-PLL-PEG:mRNA. Bar = 20 nm.

The NTA further reported on the zeta potential, which is predictive of the NP's stability within a colloidal system. The zeta potential measurements (Table 4) indicated that all functionalized NPs and their nanocomplexes were relatively stable (> 20 mV). The favorable zeta potential values further inferred the good colloidal stability of the nanocomplexes, which is essential when they are exposed to the hydrodynamic environment within a host system [42,43]. The zeta potentials of the curcumin-synthesized NPs were better than that reported previously for citrate-reduced AuNPs. [21,44]. The polydispersity index (PDI), which indicates NP size distribution, showed that all AuNPs and functionalized nanocomplexes exhibited low PDI values. Low PDIs (< 0.1) confer a uniform distribution and size, whereas high indices (> 0.4) represent a broader size distribution and dispersity, increasing the likelihood of aggregation [20,25,45]. From the results obtained, the NPs displayed favorable sizes for gene delivery and high zeta potential charges suggesting good colloidal stability. This stability was further confirmed in 3.2.

Table 4. TEM and hydrodynamic sizes, zeta potential) and polydispersity index (PDI) of all NPs and nanocomplexes at optimal binding ratios.

Nanoparticles	TEM (n=50)	NTA (n=3)					
		Nanoparticle			Nanocomplex		
	Size (nm) ± SE	Hydrodynamic size (nm) ± SE	Zeta Potential (mV) ± SE	PDI	Size (nm) ± SE	Zeta Potential (mV) ± SE	PDI
0.25 mM Curcumin							
AuNP	12.58 ± 3.6	70.0 ± 3.8	-24.4 ± 0.2	0.06±0.001	-	-	-
AuNP-PLL	13.47 ± 1.8	96.5 ± 1.1	37.1 ± 0.6	0.03±0.014	126.9 ± 4.3	-34.0 ± 0.2	0.01 ± 0.019
AuNP-PLL-PEG	13.57 ± 0.6	103 ± 24.6	36.8 ± 0.8	0.155±0.021	138.2 ± 4.2	-31.8 ± 6.5	0.044 ± 0.008
0.5 mM Curcumin							
AuNP	11.89 ± 1.9	64.7 ± 8.5	-19.6 ± 5.2	0.092 ± 0.041	-	-	-
AuNP-PLL	12.22 ± 3.3	104.8 ± 12.1	34.3 ± 4.9	0.013 ± 0.012	125.7 ± 5.8	-34.1 ± 1.4	0.017 ± 0.001
AuNP-PLL-PEG	12.87 ± 2.1	147 ± 8.0	36.1 ± 2.8	0.003 ± 0.095	153.9 ± 7.8	-29.5 ± 5.7	0.039 ± 0.003
0.75 mM Curcumin							
AuNP	11.84 ± 2.6	84.3 ± 9.2	-30.2 ± 1.2	0.009 ± 0.004	-	-	-
AuNP-PLL	11.81 ± 0.2	82.7 ± 6.8	31.5 ± 5.1	0.026 ± 0.001	103.5 ± 5.2	-30.8 ± 1.1	0.019 ± 0.009
AuNP-PLL-PEG	12.5 ± 2.4	107.4 ± 7.2	35.3 ± 4.2	0.016 ± 0.008	112.7 ± 5.8	-29.7 ± 4.7	0.025 ± 0.002
1 mM Curcumin							
AuNP	11.89 ± 1.9	74.4 ± 10.0	-34.9 ± 0.1	0.018 ± 0.020	-	-	-
AuNP-PLL	11.95 ± 2.7	73.8 ± 9.3	35.2 ± 0.9	0.016 ± 0.040	88.8 ± 2.3	-27.3 ± 2.8	0.019 ± 0.009
AuNP-PLL-PEG	12.19 ± 3.2	120.8 ± 15.7	37.5 ± 0.7	0.017 ± 0.052	129.5 ± 6.3	-30.8 ± 5.7	0.16 ± 0.008

3.2. Stability studies.

It is crucial to consider the stability of these curcumin-capped AuNPs for future *in vivo* applications. The stability of the NPs was evaluated by monitoring the change in wavelength and zeta potential of the NPs over 9 months (Figure 4). The wavelength change was found to be ±5 nm, while the change in zeta potential was less than 3 mV indicating that these NPs were stable and had a long shelf life which bodes well for their future *in vivo* use [21]. This demonstrated long-term stability is essential for therapeutic and economic purposes. The bioprotective property of curcumin stems from its distinct chemical structure. Several reports have shown the ability of curcumin to inhibit the generation of free radicals [19,34,46]. Although some studies have suggested optimal molar ratios of 1: 4 for AuNPs synthesis with a λ_{max} at 528 nm [33,47], our results indicated that the 1:1 molar ratio of curcumin to HAuCl₄ with a λ_{max} at 525 nm generated favorable NP sizes, excellent zeta potentials, and good stability.

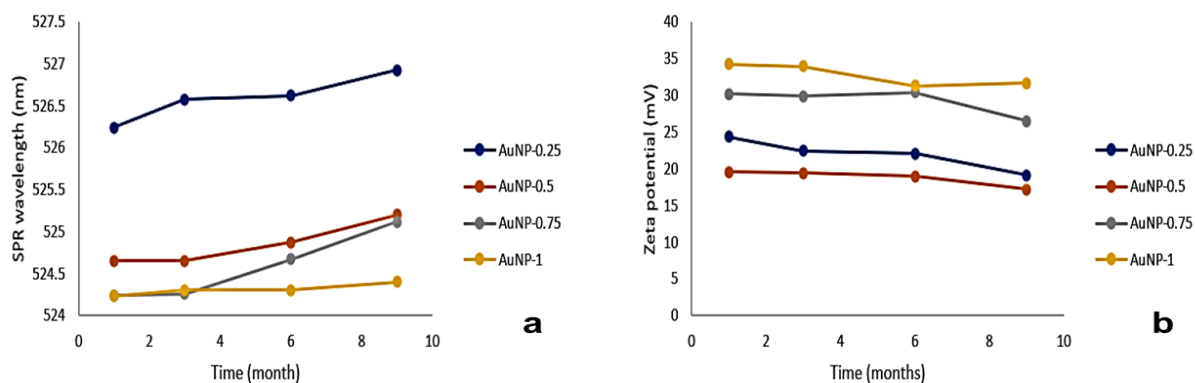


Figure 4. Stability graph for (a) wavelength and (b) zeta potential of curcumin synthesized AuNPs in aqueous solution over nine months.

3.3 Band-shift assay.

The application of mRNA in cancer immunotherapy has revolutionized the pharmaceutical industry by eliminating limitations in recombinant protein synthesis where desired transient expression is required [48,49]. The band-shift was conducted to determine the minimum amount ($\mu\text{g}/\mu\text{L}$) of functionalized and PEGylated NPs that were required to bind to $0.3 \mu\text{g}/\mu\text{L}$ of mRNA fully. These weight ratios were determined through the electrostatic interactions between the negatively charged mRNA molecule and positively charged NPs. As a result, the concentration of the mRNA remained constant, whereas the mass of the NP increased in uniform intervals until an electroneutral complex was formed, resulting in the nanocomplex remaining in the well instead of migrating into the agarose gel matrix (Figure 5).

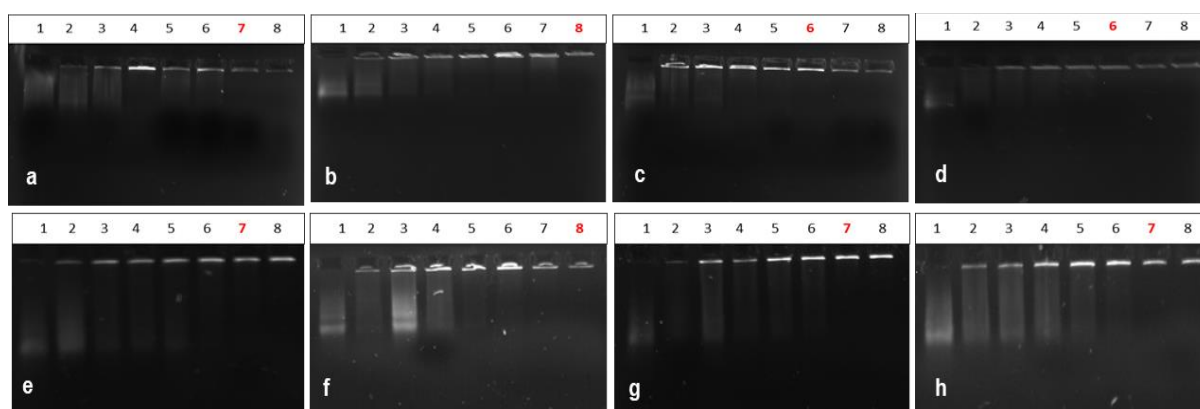


Figure 5. Gel retardation assay of mRNA-nanocomplexes prepared using increasing amounts of NPs (Lanes 2-8: 0.06, 0.12, 0.18, 0.24, 0.30, 0.36 and $0.42 \mu\text{g}$) and a fixed amount of mRNA ($0.3 \mu\text{g}$). Lane 1: Control ($0.3 \mu\text{g}$ mRNA). AuNP-0.25-PLL (a), AuNP-0.5-PLL (b), AuNP-0.75-PLL (c), AuNP-1-PLL (d), AuNP-0.25-PLL-PEG (e), AuNP-0.5-PLL-PEG (f), AuNP-0.75-PLL-PEG (g), AuNP-1-PLL-PEG: *FLuc*-mRNA complexes (h). Wells labeled in red indicate complete binding.

The ratio at which the minimum amount of NP is needed to bind the mRNA completely is referred to as the optimum binding ratio. The ratio below this is referred to as the sub-optimum binding ratio, and the ratio above the optimum ratio is referred to as the supra-optimum binding ratio. All NPs were able to bind to the mRNA at relatively low ratios. The AuNPs synthesized used 0.75 mM and 1 mM curcumin produced low binding ratios (w/w). Lower binding ratios are significant since high concentrations of gold can induce oxidative damage to kidney and liver cells *in vivo* [50,51]. The AuNP-PLL has a higher binding affinity due to the greater availability of cationic amine groups (positive charges), which electrostatically bound the negatively charged mRNA [52].

3.4. Dye displacement assay.

In addition to favorable binding, the compaction of the mRNA should be tight enough to ensure that it does not dissociate prematurely from the nanocarrier and degrade but not too strong that it would prevent unpacking and lower transfection efficiency [49]. The EB intercalation assay showed that gradually adding the AuNPs resulted in the displacement of the EB as the positive charges of the PLL bound to the negative charges of the mRNA. This assay has been used extensively to examine the ability of the cationic NPs to condense and compact nucleic acids. EB fluoresces when it intercalates between the bases of the mRNA. This fluorescence was taken as 100% fluorescence [25]. A stepwise decrease in fluorescence was observed as the NPs bound to the mRNA, displacing the bound dye (Figure 6). This was due

to the incremental addition of the NPs, resulting in the conformation of the mRNA structure changing as it bound to the NPs. Hence, the affinity for the dye was reduced, resulting in a decline in fluorescence. The functionalized NPs efficiently condensed and compacted the mRNA at varying degrees [20]. All NPs exhibited a fluorescence decay greater than 50%. AuNP-PLL displayed a compaction ability of 55 - 97%, whereas the AuNP-PLL-PEG showed a slightly lower higher compaction ability between 50% and 95%. The 0.75 mM and 1 mM curcumin AuNPs produced higher compaction.

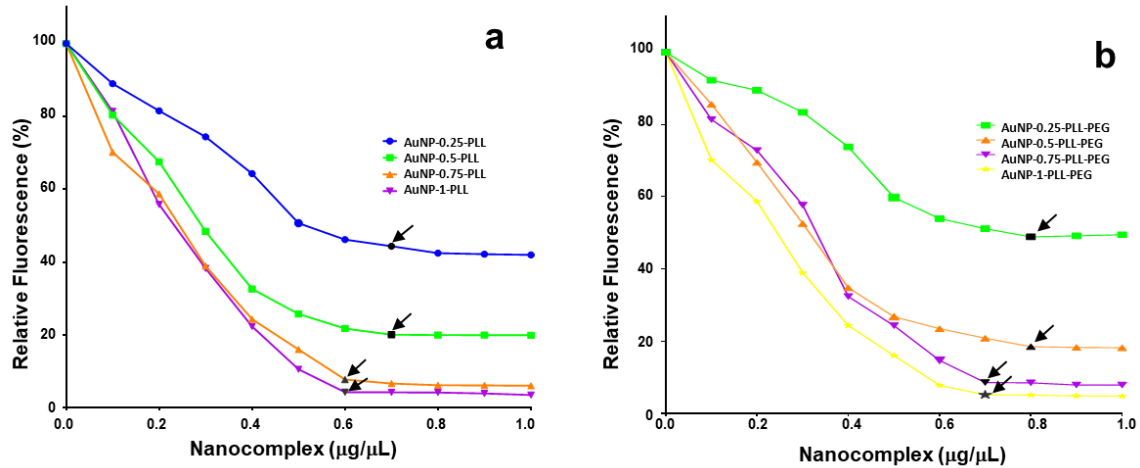


Figure 6. Ethidium bromide intercalation assay of functionalized AuNPs. (a) AuNP-PLL and (b) AuNP-PLL-PEG. Black points and arrows indicate the point of inflection.

3.5 mRNA protection assay.

Under physiological conditions, AuNPs are subjected to various interactions with biomolecules such as serum proteins. These interactions may affect the NP's stability, physicochemical properties, or biological responses [21,53]. In this regard, the nuclease protection assays served to highlight the protective abilities of these AuNPs to their nucleic acid cargo. The positive control (P) showed a distinct single band that indicated undigested mRNA, while the negative control (N) did not show a band, indicating complete digestion of the nucleic acid (Figure 7). All nanocomplexes generated a distinct band similar to the positive control, confirming the ability of the functionalized AuNPs to protect the mRNA [20,37,54], boding well for *in vivo* delivery.

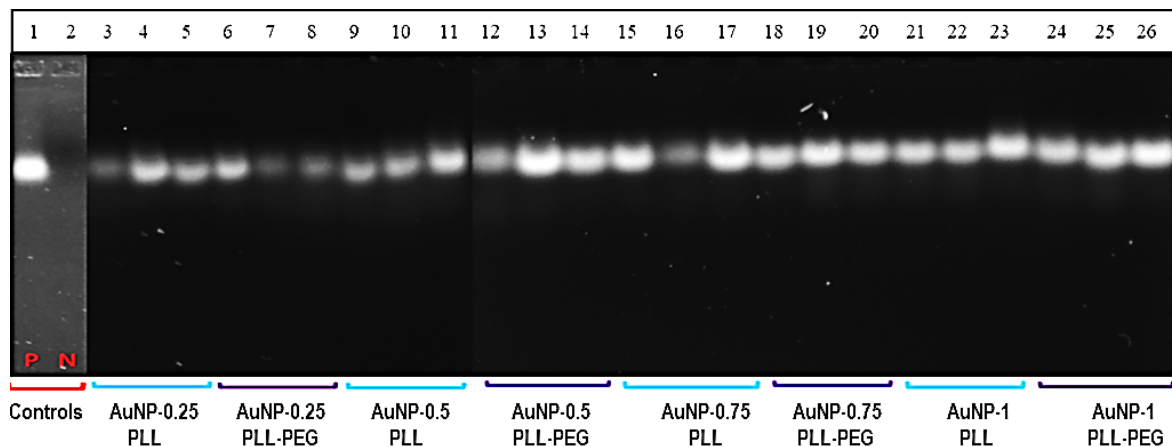


Figure 7. The enzyme protection assay of the AuNP: FLuc-mRNA nanocomplexes at their sub-optimum, optimum, and supra-optimum ratios (lanes 1,2,3 and 4,5,6, respectively). P=positive control (untreated mRNA) and N= negative control (FBS-treated mRNA).

3.6 MTT cell viability assay.

Previous reports have shown that AuNPs synthesized by chemical or physical means have induced significant toxicity to non-malignant cells. Metallic nanoparticles may adhere to and damage cell walls and membranes due to the steady release of ions [55]. This study, together with previous literature, confirms that green synthesized NPs have better biocompatibility than chemically synthesized NPs due to the phytochemicals within the curcumin producing a non-toxic coating on the AuNPs [9]. The cytotoxicity of the nanocomplexes was evaluated in the HeLa and HEK293 cells using the MTT (3-(4,5-dimethylthiazol-2-yl)-2,5-diphenyl tetrazolium bromide) assay, which measures the metabolic activity of the cell. The assay converts the yellow MTT salt into a purple formazan product using the mitochondrial dehydrogenase enzyme found in living cells. The quantity of formazan product is directly proportional to the number of viable cells and inversely proportional to the degree of cytotoxicity [21, 56]. The results are expressed as the percentage of cell viability against the control (100%). Figure 8 shows that all nanocomplexes were well tolerated in the HeLa and HEK293 cells. The HEK293 cells were used as a model for kidney cells since NPs tend to accumulate in the kidneys following systematic administration [57]. All nanocomplexes displayed favorable cell viability (> 88%) in the HEK293 cells, suggesting that they will not produce renal toxicity *in vivo*. However, higher toxicities in cancer cells were reported [58,59]. Although the NPs were well tolerated in the HeLa cells, a slight reduction in cell viability (> 70%) was observed, which could be attributed to the anticancer properties of curcumin [60]. Curcumin acts as a blocking agent altering the transcription factors, oncogenes, and signaling proteins, which facilitates cancer cells' growth and metastasis at different stages of carcinogenesis [61,62]. Furthermore, the unsaturated heptadiene chain of curcumin inhibits the transcription factor of nuclear factor-kappa (NF-κB), BCL-2, cyclin D1, c-MYC, and TNFα, giving curcumin its anticarcinogenic properties [63].

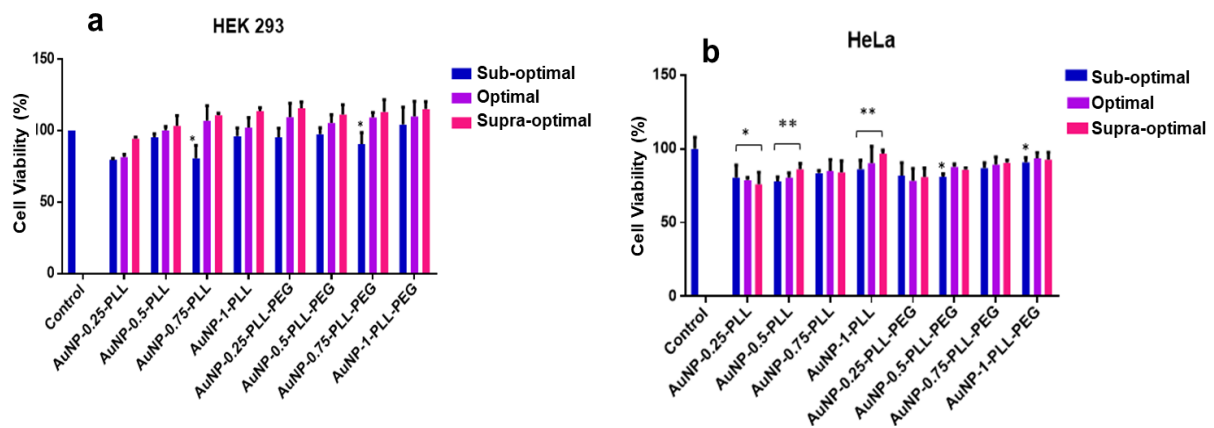


Figure 8. Cytotoxicity in the (a) HEK293 and (b) HeLa cells. Data are represented as means \pm SD (n=3). *p<0.05 and **p<0.01 were considered statistically significant between the corresponding means of each sub-optimal, optimum, and supra-optimal nanocomplexes and the positive control (Tukey's multiple comparisons test).

3.7. Luciferase reporter gene assay.

The transfection efficiency of the nanocomplexes was assessed using the luciferase reporter gene assay (Figure 9). All the nanocomplexes elicited significant mRNA expression in both cell lines, with the luciferase activity higher than that of mRNA alone. The nanocomplexes with the best stability and cellular uptake contained 0.75 mM and 1 mM

curcumin. Nanocomplex properties such as the favorable size, good zeta potential, protection of mRNA from nucleases, and low cytotoxicity further enhanced cellular uptake of the nanocomplexes [21,25]. The PEGylated NPs showed better luciferase activity than their AuNP-PLL counterparts, with the nanocomplexes containing 1 mM curcumin displaying the best transfection efficiency in both cell lines. The hydrophilic nature and low surface energy of PEG can create steric repulsion and form a hydrated cloud around the nanocomplex, allowing it to evade foreign substances, opsonization, and premature phagocytosis, further increasing its biocompatibility [32,64]. This promotes successful delivery to the TME by increasing the circulation time of the nanocarriers within the body [21]. Overall, these AuNPs depicted higher cellular uptake in HeLa cells than in HEK293 cells, suggesting a degree of cell specificity.

Although the formulation of curcumin-conjugated nanoparticles has tremendously improved curcumin's bioavailability, there are still several issues to be addressed regarding its potency and specificity. As a result of the low efficacy, higher doses are required to achieve a therapeutic response, which increases the adverse effects and reduces patient compliance. Furthermore, there is a lack of clinical studies to evaluate the safety and efficacy of these curcumin delivery systems in humans. Current drug delivery systems for curcumin lack cell specificity. Tissue-specific curcumin delivery would enhance the drug concentration at the target site, producing higher efficacy (with lower doses of curcumin) and fewer adverse effects. Cell specificity can be induced by employing targeting moieties such as folic acid (FA), which has displayed great promise as a stabilizing agent due to its biocompatibility, cell proliferation, replication control, and synthesis of proteins [25]. Moreover, it has a high affinity toward FA receptors which are overexpressed in breast and cervical cells [49,54,59,65,66].

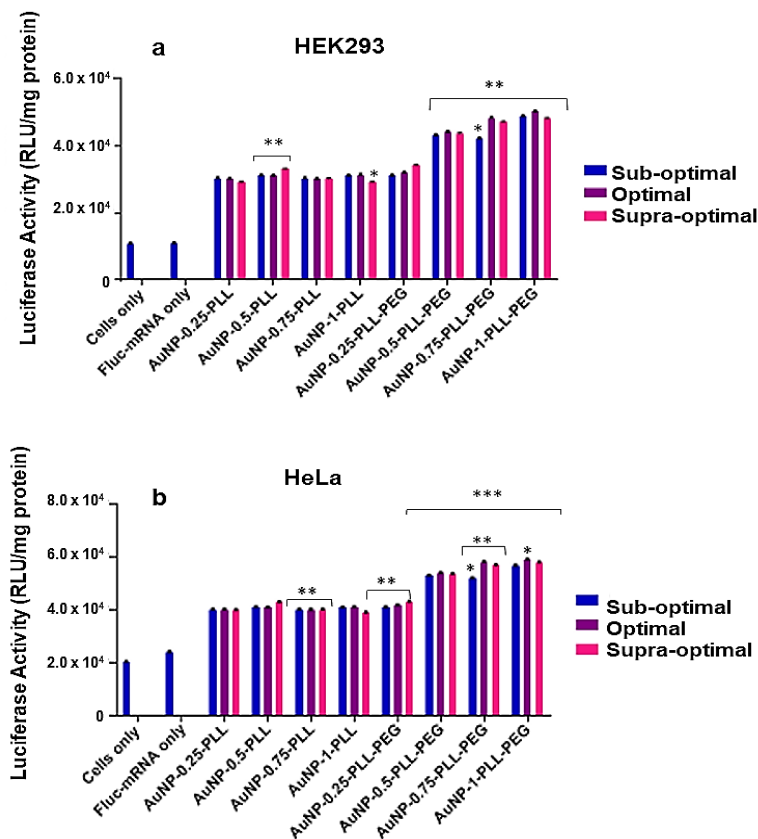


Figure 9. Luciferase activity in (a) HEK293 and (b) HeLa cells. Data are represented as means \pm SD (n=3). *p<0.05 and ***p<0.001, and **p<0.01, considered statistically significant between the corresponding means of each of the sub-optimal, optimum, and supra-optimal nanocomplexes and the positive control (Tukey's multiple comparison test).

4. Conclusions

AuNPs have become increasingly popular due to their appealing physical, chemical, and biological properties. Their synthesis via green chemistry has gained momentum in recent years. This research was carried out on a cervical cell model as a proof-of-concept study to determine which concentration of curcumin used in capping the AuNPs was superior in gene delivery. The study confirmed curcumin's ability to be solubilized at an alkaline pH without using any external agent and to reduce and stabilize H₂AuCl₄ to form AuNPs. The size and dispersity of the AuNPs can be controlled by varying the concentration of curcumin. All the synthesized curcumin encapsulated AuNPs were stable for up to nine months under ambient conditions, allowing them to be stored over long periods, which is attractive for commercialization. All nanocomplexes were non-toxic, protected the mRNA, induced favorable transgene expression, and hence showed great potential as vehicles for facilitating mRNA delivery. The use of mRNA in a vaccine was highlighted during the COVID-19 pandemic, and novel systems such as this are central to furthering their use in vaccinations for other diseases. Overall, the 1 mM curcumin-capped AuNP demonstrated the highest transgene expression and would be chosen for further studies. Although there is still limited knowledge of the long-term risks of curcumin, these curcumin-capped AuNPs provide an exciting prospect for use in gene or drug delivery studies.

Funding

This research was funded by the National Research Foundation (NRF), South Africa (Grant no: 120455).

Acknowledgments

The authors acknowledge members of the Nano-Gene and Drug Delivery Laboratory for technical support.

Conflicts of Interest

The authors declare no conflict of interest.

References

1. Venkatas, J.; Singh, M. Nanomedicine-mediated optimization of immunotherapeutic approaches in cervical cancer. *Nanomedicine* **2021**, *16*, 1311–1328, <https://doi.org/10.2217/nnm-2021-0044>.
2. Zhang, H.; Li, T.; Luo, W.; Peng, G. X.; Xiong, J. Green synthesis of Ag nanoparticles from *Leucus aspera* and its application in anticancer activity against alveolar cancer. *J. Exp. Nanosci.* **2022**, *17*, 47–60, <https://doi.org/10.1080/17458080.2021.2007886>.
3. Kumari, M.; Sharma, N.; Manchanda, R.; Gupta, N.; Syed, A.; Bahkali, A. H.; Nimesh, S. PGMD/curcumin nanoparticles for the treatment of breast cancer. *Sci. Rep.* **2021**, *11*, 1–7, <https://doi.org/10.1038/s41598-021-81701-x>.
4. Venkatas, J.; Singh, M. Cervical cancer: a meta-analysis, therapy and future of nanomedicine. *Ecancermedicalscience* **2020**, *14*, 1111–1128, <https://doi.org/10.3332/ecancer.2020.1111>.
5. Boomi, P.; Poorani, G. P.; Selvam, S.; Palanisamy, S.; Jegatheeswaran, S.; Anand, K.; Balakumar, C.; Premkumar, K.; Prabu, H. G. Green biosynthesis of gold nanoparticles using *Croton sparsiflorus* leaves extract and evaluation of UV protection, antibacterial and anticancer applications. *Appl. Organomet. Chem.* **2020**, *34*, e5574, <https://doi.org/10.1002/aoc.5574>.

6. Aswini, R.; Murugesan, S.; Kannan, K. Bio-engineered TiO₂ nanoparticles using *Ledebouria revoluta* extract: *Larvicidal*, histopathological, antibacterial and anticancer activity. *Int. J. Environ. Anal. Chem.* **2021**, *101*, 2926–2936, <https://doi.org/10.1080/03067319.2020.1718668>.
7. Rohini, B.; Akther, T.; Waseem, M.; Khan, J.; Kashif, M.; Hemalatha, S. AgNPs from *Nigella sativa* control breast cancer: an *in vitro* study. *J Environ Pathol Toxicol Oncol.* 2019; *38*, 185–94. <https://doi.org/10.1615/JEnvironPatholToxicolOncol.2019027318>.
8. Saranya, T. S.; Rajan, V. K.; Biswas, R.; Jayakumar, R.; Sathianarayanan, S. Synthesis, characterization and biomedical applications of curcumin conjugated chitosan microspheres. *Int. J. Biol. Macromol.* **2018**, *110*, 227–233, <https://doi.org/10.1016/j.ijbiomac.2017.12.044>.
9. Yang, Q. Q.; Farha, A. K.; Kim, G.; Gul, K.; Gan, R. Y.; Corke, H. Antimicrobial and anticancer applications and related mechanisms of curcumin-mediated photodynamic treatments. *Trends Food Sci. Technol.* **2020**, *97*, 341–354, <https://doi.org/10.1016/j.tifs.2020.01.023>.
10. Ferrari, R.; Sponchioni, M.; Morbidelli, M.; Moscatelli, D. Polymer nanoparticles for the intravenous delivery of anticancer drugs: the checkpoints on the road from the synthesis to clinical translation. *Nanoscale* **2018**, *10*, 22701–22719, <https://doi.org/10.1039/C8NR05933K>.
11. Duse, L.; Agel, M. R.; Pinnapireddy, S. R.; Schäfer, J.; Selo, M. A.; Ehrhardt, C.; Bakowsky, U. Photodynamic Therapy of Ovarian Carcinoma Cells with Curcumin-Loaded Biodegradable Polymeric Nanoparticles. *Pharmaceutics* **2019**, *11*, 282, <https://doi.org/10.3390/pharmaceutics11060282>.
12. Elbially, N. S.; Abdelfatah, E. A.; Khalil, W. A. Antitumor activity of curcumin-green synthesized gold nanoparticles: *in vitro* study. *Bionanoscience* **2019**, *9*, 813–820, <https://doi.org/10.1007/s12668-019-00660-w>.
13. Liu, R.; Pei, Q.; Shou, T.; Zhang, W.; Hu, J.; Li, W. Apoptotic effect of green synthesized gold nanoparticles from *Curcuma wenyujin* extract against human renal cell carcinoma A498 cells. *Int. J. Nanomedicine* **2019**, *14*, 4091–4103, <https://doi.org/10.2147/IJN.S203222>.
14. Ubeyitogullari, A.; Ciftci, O. N. A novel and green nanoparticle formation approach to forming low-crystallinity curcumin nanoparticles to improve curcumin's bioaccessibility. *Sci. Rep.* **2019**, *9*, 1–11, <https://doi.org/10.1038/s41598-019-55619-4>.
15. Venkatas, J.; Daniels, A.; Singh, M. The Potential of Curcumin-Capped Nanoparticle Synthesis in Cancer Therapy: A Green Synthesis Approach. *Nanomaterials* **2022**, *12*, 3201, <https://doi.org/10.3390/nano12183201>.
16. Zhou, J.; Cao, Z.; Panwar, N.; Hu, R.; Wang, X.; Qu, J.; Tjin, S. C.; Xu, G.; Yong, K.-T. Functionalized gold nanorods for nanomedicine: Past, present and future. *Coord. Chem. Rev.* **2017**, *352*, 15–66, <https://doi.org/10.1016/j.ccr.2017.08.020>.
17. Li, B.; Lane, L. A. Probing the biological obstacles of nanomedicine with gold nanoparticles. *Wiley Interdiscip. Rev. Nanomed. Nanobiotechnol.* **2019**, *11*, 1542, <https://doi.org/10.1002/wnan.1542>.
18. Rejinold, N.S.; Thomas, R.G.; Muthiah, M.; Chennazhi, K.; Manzoor, K.; Park, I.K.; *et al.* Anti-cancer, pharmacokinetics and tumor localization studies of pH-, RF- and thermo-responsive nanoparticles. *Int J Biol Macromol.* **2015**, *74*, 249–62, <https://doi.org/10.1016/j.ijbiomac.2014.11.044>.
19. Nambiar, S.; Osei, E.; Fleck, A.; Darko, J.; Mutsaers, A. J.; Wettig, S. Synthesis of curcumin-functionalized gold nanoparticles and cytotoxicity studies in human prostate cancer cell line. *Appl. Nanosci.* **2018**, *8*, 347–357, <https://doi.org/10.1007/s13204-018-0728-6>.
20. Naidoo, S.; Daniels, A.; Habib, S.; Singh, M. Poly-L-Lysine–Lactobionic Acid-Capped Selenium Nanoparticles for Liver-Targeted Gene Delivery. *Int. J. Mol. Sci.* **2022**, *23*, 1492, <https://doi.org/10.3390/ijms23031492>.
21. Daniels, A. N.; Singh, M. Sterically stabilized siRNA: gold nanocomplexes enhance c-MYC silencing in a breast cancer cell model. *Nanomedicine* **2019**, *14*, 1387–1401, <https://doi.org/10.2217/nnm-2018-0462>.
22. Lee, N.K.; Park, S.S.; Ha, C.S. pH-sensitive drug delivery system based on mesoporous silica modified with Poly-L-Lysine (PLL) as a Gatekeeper. *J Nanosci Nanotechnol.* **2020**, *20*, 6925–34, <https://doi.org/10.1166/jnn.2020.18821>.
23. Barrios-Gumiel, A.; Sanchez-Nieves, J.; Perez-Serrano, J.; Gomez, R.; de la Mata, F. J. PEGylated AgNP covered with cationic carbosilane dendrons to enhance antibacterial and inhibition of biofilm properties. *Int. J. Pharm.* **2019**, *569*, 118591, <https://doi.org/10.1016/j.ijpharm.2019.118591>.
24. Singh, M. Assessing Nucleic acid: Cationic Nanoparticle Interaction for Gene Delivery. In *Bio-Carrier Vectors*, N. Kumaran (Ed), Springer-Nature, New York, NY, USA; **2021**, *2211*, 43–55, https://doi.org/10.1007/978-1-0716-0943-9_4.

25. Joseph, C.; Daniels, A.; Singh, S.; Singh, M. Histidine-Tagged Folate-Targeted Gold Nanoparticles for Enhanced Transgene Expression in Breast Cancer Cells *In vitro*. *Pharmaceutics* **2022**, *14*, 53, <https://doi.org/10.3390/pharmaceutics14010053>.
26. Sindhu, K.; Rajaram, A.; Sreeram, K. J.; Rajaram, R. Curcumin conjugated gold nanoparticle synthesis and its biocompatibility. *RSC Advances* **2014**, *4*, 1808–1818, <https://doi.org/10.1039/C3RA45345F>.
27. Khodashenas, B.; Ardjmand, M.; Rad, A.S.; Esfahani, M.R. Gelatin-coated gold nanoparticles as an effective pH-sensitive methotrexate drug delivery system for breast cancer treatment. *Mater. Today Chem.* **2021**, *2*, 100474, <https://doi.org/10.1016/j.mtchem.2021.100474>.
28. Samadian, H.; Hosseini-Nami, S.; Kamrava, S. K.; Ghaznavi, H.; Shakeri-Zadeh, A. Folate-conjugated gold nanoparticle as a new nanoplatform for targeted cancer therapy. *J. Cancer Res. Clin. Oncol.* **2016**, *142*, 2217–2229, <https://doi.org/10.1007/s00432-016-2179-3>.
29. He, Y.; Yang, M.; Zhao, S.; Cong, C.; Li, X.; Cheng, X.; Yang, J.; Gao, D. Regulatory mechanism of localized surface plasmon resonance based on gold nanoparticles-coated paclitaxel nanoliposomes and their antitumor efficacy. *ACS Sustain. Chem. & Eng.* **2018**, *6*, 13543–13550, <https://doi.org/10.1021/acssuschemeng.8b03711>.
30. Singh, P.; Pandit, S.; Mokkapati, V. R.; Garg, A.; Ravikumar, V.; Mijakovic, I. Gold Nanoparticles in Diagnostics and Therapeutics for Human Cancer. *Int. J. Mol. Sci.* **2018**, *19*, 1979, <https://doi.org/10.3390/ijms19071979>.
31. Dong, Y. C.; Hajfathalian, M.; Maidment, P. S.; Hsu, J. C.; Naha, P. C.; Si-Mohamed, S.; Breuille, M.; Kim, J.; Chhour, P.; Douek, P.; *et al.* effect of gold nanoparticle size on their properties as contrast agents for computed tomography. *Sci. Rep.* **2019**, *9*, 1–13, <https://doi.org/10.1038/s41598-019-50332-8>.
32. Xu, B.; Li, A.; Hao, X.; Guo, R.; Shi, X.; Cao, X. PEGylated dendrimer-entrapped gold nanoparticles with low immunogenicity for targeted gene delivery. *RSC Advances* **2018**, *8*, 1265–1273, <https://doi.org/10.1039/C7RA11901A>.
33. Sreelakshmi, C.; Goel, N.; Datta, K. K.; Addlagatta, A.; Ummanni, R.; Reddy, B. V. Green synthesis of curcumin capped gold nanoparticles and evaluation of their cytotoxicity. *Nanosci. Nanotechnol. Lett.* **2013**, *5*, 1258–1265, <https://doi.org/10.1166/nml.2013.1678>.
34. Wulandari, T.; Nagahiro, T.; Fukada, N.; Kimura, Y.; Niwano, M.; Tamada, K.; Nagahiro, N.; Fukada, Y.; Kimura, M.; Tamada, K. Characterization of citrates on gold and silver nanoparticles. *J Colloid Interface Sci.* **2015**; *438*, 244–8, <https://doi.org/10.1016/j.jcis.2014.09.078>.
35. Tam, S. K.; Dusseault, J.; Polizu, S.; Ménard, M.; Hallé, J. P.; Yahia, L. Physicochemical model of alginate–poly-L-lysine microcapsules defined at the micrometric/nanometric scale using ATR-FTIR, XPS, and ToF-SIMS. *Biomaterials* **2005**, *26*, 6950–6961, <https://doi.org/10.1016/j.biomaterials.2005.05.007>.
36. Luo, Q.; Gao, H.; Peng, L.; Liu, G.; Zhang, Z. Synthesis of PEGylated chitosan copolymers as efficiently antimicrobial coatings for leather. *J. Appl. Polym. Sci.* **2016**, *133*, 64, <https://doi.org/10.1002/app.43465>.
37. Huo, S.; Jin, S.; Ma, X.; Xue, X.; Yang, K.; Kumar, A.; Wang, P. C.; Zhang, J.; Hu, Z.; Liang, X.-J. Ultrasmall gold nanoparticles as carriers for nucleus-based gene therapy due to size-dependent nuclear entry. *ACS Nano* **2014**, *8*, 5852–5862, <https://doi.org/10.1021/nn5008572>.
38. Das, T.; Mishra, S.; Nag, S.; Saha, K.D. Green-synthesized gold nanoparticles from black tea extract enhance the chemosensitivity of doxorubicin in HCT116 cells via a ROS-dependent pathway. *RSC Advances.* **2022**; *12*, 8996–9007, <https://doi.org/10.1039/D1RA08374K>.
39. Akbari, A.; Shokati Eshkiki, Z.; Mayahi, S.; Amini, S. M. In-vitro investigation of curcumin coated gold nanoparticles effect on human colorectal adenocarcinoma cell line. *J. Nanomed. Res.* **2022**, *7*, 66–72, http://www.nanomedicine-rj.com/article_251671.html.
40. Deepak, P.; Amutha, V.; Kamaraj, C.; Balasubramani, G.; Aiswarya, D.; Perumal, P. Chemical and green synthesis of nanoparticles and their efficacy on cancer cells. In *Green Synth., Characterization App. Nano* **2019**, 369–387, Elsevier, <https://doi.org/10.1016/B978-0-08-102579-6.00016-2.v>
41. Aboyewa, J. A.; Sibuyi, N. R.; Meyer, M.; Oguntibeju, O. O. Green synthesis of metallic nanoparticles using some selected medicinal plants from Southern Africa and their biological applications. *Plants* **2021**, *10*, 1929, <https://doi.org/10.3390/plants10091929>.
42. Forest, V.; Pourchez, J. Preferential binding of positive nanoparticles on cell membranes is due to electrostatic interactions: A too simplistic explanation that does not take into account the nanoparticle protein corona. *Mater. Sci. Eng. C* **2017**, *70*, 889–896, <https://doi.org/10.1016/j.msec.2016.09.016>.

43. Park, S.; Lee, W. J.; Park, S.; Choi, D.; Kim, S.; Park, N. Reversibly pH-responsive gold nanoparticles and their applications for photothermal cancer therapy. *Sci. Rep.* **2019**, *9*, 1–9, <https://doi.org/10.1038/s41598-019-56754-8>.
44. David, S.; Patel, D.Y.; Cardona, S.; Kirby, N.; Mayer, K.M. Cellular Uptake and Cytotoxicity of PEGylated Gold Nanoparticles in C33A Cervical Cancer Cells. *Nano Express.* **2022**, *3*, 9, <https://doi.org/10.1088/2632-959X/ac7738>.
45. Clayton, K. N.; Salameh, J. W.; Wereley, S. T.; Kinzer-Ursem, T. L. Physical characterization of nanoparticle size and surface modification using particle scattering diffusometry. *Biomicrofluidics* **2016**, *10*, 054107, <https://doi.org/10.1063/1.4962992>.
46. Akhtar, S.; Asiri, S. M.; Khan, F. A.; Gunday, S. T.; Iqbal, A.; Alrushaid, N.; Labib, O. A.; Deen, G. R.; Henari, F. Z. Formulation of gold nanoparticles with hibiscus and curcumin extracts induced anticancer activity. *Arab. J. Chem.* **2022**, *15*, 103594, <https://doi.org/10.1016/j.arabjc.2021.103594>.
47. Prasad, M.; Salar, A.; Salar, R. K. *In vitro* anticancer activity of curcumin loaded chitosan nanoparticles (CLCNPs) against Vero cells. *Pharmacol. Res.* **2022**, *3*, 100116, <https://doi.org/10.1016/j.prmcm.2022.100116>.
48. Weng, Y.; Li, C.; Yang, T.; Hu, B.; Zhang, M.; Guo, S.; Xiao, H.; Liang, X.-J.; Huang, Y. The challenge and prospect of mRNA therapeutics landscape. *Biotechnol. Adv.* **2020**, *40*, 107534, <https://doi.org/10.1016/j.biotechadv.2020.107534>.
49. Maiyo, F.; Singh, M. Folate-targeted mRNA delivery using chitosan-functionalized selenium nanoparticles: potential in cancer immunotherapy. *Pharmaceuticals (Basel)* **2019**, *12*, 164–178, <https://doi.org/10.3390/ph12040164>.
50. Enea, M.; Pereira, E.; Costa, J.; Soares, M. E.; da Silva, D. D.; de Lourdes Bastos, M.; *et al.* Cellular uptake and toxicity of gold nanoparticles on two distinct hepatic cell models. *Toxicol. In vitro* **2021**, *70*, 105046, <https://doi.org/10.1016/j.tiv.2020.105046>.
51. Sani, A.; Cao, C.; Cui, D. Toxicity of gold nanoparticles (AuNPs): A review. *Biochem. Biophys. Rep.* **2021**, *26*, 100991, <https://doi.org/10.1016/j.bbrep.2021.100991>.
52. Hasanzadeh, A.; Jahromi, M. A.; Abdoli, A.; Mohammad-Beigi, H.; Fatahi, Y.; Nourizadeh, H.; *et al.* Photoluminescent carbon quantum dot/poly-L-Lysine core-shell nanoparticles: A novel candidate for gene delivery. *J. Drug Deliv. Sci. Technol.* **2021**, *61*, 102118, <https://doi.org/10.1016/j.jddst.2020.102118>.
53. Amani, A.; Alizadeh, M. R.; Yaghoubi, H.; Ebrahimi, H. A. Design and fabrication of novel multi-targeted magnetic nanoparticles for gene delivery to breast cancer cells. *J. Drug Deliv. Sci. Technol.* **2021**, *61*, 102151, <https://doi.org/10.1016/j.jddst.2020.102151>.
54. Mbatha, L. S.; Maiyo, F.; Daniels, A.; Singh, M. Dendrimer-Coated Gold Nanoparticles for Efficient Folate-Targeted mRNA Delivery *In vitro*. *Pharmaceutics* **2021**, *13*, 900, <https://doi.org/10.3390/pharmaceutics13060900>.
55. Menon, S.; Shanmugam, R.; Kumar, V. A review on biogenic synthesis of gold nanoparticles, characterization, and its applications. *Resource-Efficient Technologies.* **2017**, *3*, 516–27, <https://doi.org/10.1016/j.reffit.2017.08.002>.
56. Amale, F. R.; Ferdowsian, S.; Hajrasouliha, S.; Kazempoor, R.; Mirzaie, A.; Dakkali, M. S.; *et al.* Gold nanoparticles loaded into niosomes: A novel approach for enhanced antitumor activity against human ovarian cancer. *Adv. Powder Technol.* **2021**, *32*, 4711–4722, <https://doi.org/10.1016/j.apt.2021.10.019>.
57. Achilli, C.; Ciana, A.; Minetti, G. Immortalized HEK 293 kidney cell lines as models of renal cells: friends or foes? *J. Controversies Biomed Res* **2018**, *4*, 6–9, <https://doi.org/10.15586/jcbmr.2018.26>.
58. Daei, S.; Pourkabirah, R.A.A.; Majidi, N.Z. Investigating Anticancer Effects of Silver Nanoparticles on Bladder Cancer 5637 Cells in Comparison to Human Embryonic Kidney Normal Cells (HEK-293). *Armaghane Danesh.* **2022**, *10*, 27–41, <http://armaghanj.yums.ac.ir/article-1-3128-en.html>.
59. Akinyelu, J.; Singh, M. Folate-tagged chitosan-functionalized gold nanoparticles for enhanced delivery of 5-fluorouracil to cancer cells. *Appl. Nanosci.* **2019**, *9*, 7–17, <https://doi.org/10.1007/s13204-018-0896-4>.
60. Vemuri, S. K.; Halder, S.; Banala, R. R.; Rachamalla, H. K.; Devraj, V. M.; Mallarpu, C. S.; Neerudu, U. K.; Bodlapati, R.; Mukherjee, S.; Venkata, S. G. P.; *et al.* Modulatory Effects of Biosynthesized Gold Nanoparticles Conjugated with Curcumin and Paclitaxel on Tumorigenesis and Metastatic Pathways—*In vitro* and *In vivo* Studies. *Int. J. Mol. Sci.* **2022**, *23*, 2150, <https://doi.org/10.3390/ijms23042150>.
61. Tan, B.; Norhaizan, M. E. Curcumin combination chemotherapy: the implication and efficacy in cancer. *Molecules* **2019**, *24*, 2527, <https://doi.org/10.3390/molecules24142527>.

62. Perera, W. P.; Dissanayake, R. K.; Ranatunga, U. I.; Hettiarachchi, N. M.; Perera, K. D.; Unagolla, J. M.; De Silva, R. T.; Pahalagedara, L. R. curcumin loaded zinc oxide nanoparticles for activity-enhanced antibacterial and anticancer applications. *RSC Advances* **2020**, *10*, 30785–30795, <https://doi.org/10.1039/D0RA05755J>.
63. Hotsumi, M.; Tajiri, M.; Nikaido, Y.; Sato, T.; Makabe, K.; Konno, H. Design, synthesis, and evaluation of a water soluble C5-monoketone type curcumin analogue as a potent amyloid β aggregation inhibitor. *Bioorg. Med. Chem. Lett.* **2019**, *29*, 2157–2161, <https://doi.org/10.1016/j.bmcl.2019.06.052>.
64. Suk, J. S.; Xu, Q.; Kim, N.; Hanes, J.; Ensign, L. M. PEGylation as a strategy for improving nanoparticle-based drug and gene delivery. *Adv. Drug Deliv. Rev.* **2016**, *99*, 28–51, <https://doi.org/10.1016/j.addr.2015.09.012>.
65. Aljarba, N.H.; Imtiaz, S.; Anwar, N.; Alanazi, I.S., Alkahtani, S. Anticancer and microbial activities of gold nanoparticles: A mechanistic review. *J King Saud Univ Sci.* **2022**, *34*, 101907, 2022.101907. <https://doi.org/10.1016/j.jksus.2022.101907>.
66. Mahalunkar, S.; Yadav, A. S.; Gorain, M.; Pawar, V.; Braathen, R.; Weiss, S.; Bogen, B.; Gosavi, S. W.; Kundu, G. C. Functional design of pH-responsive folate-targeted polymer-coated gold nanoparticles for drug delivery and *in vivo* therapy in breast cancer. *Int. J. Nanomedicine* **2019**, *14*, 8285–8302, <https://doi.org/10.2147/IJN.S215142>.

Supplementary Material

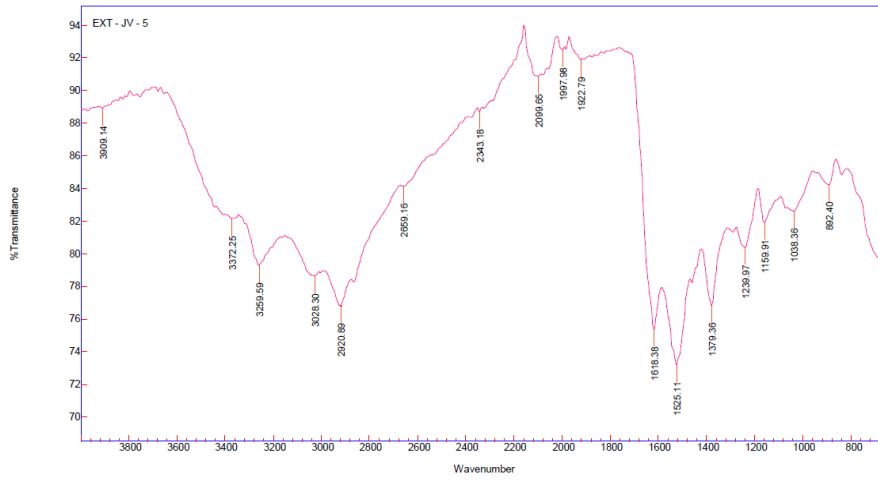


Figure S1. FTIR spectra of curcumin synthesized AuNP (1mM).

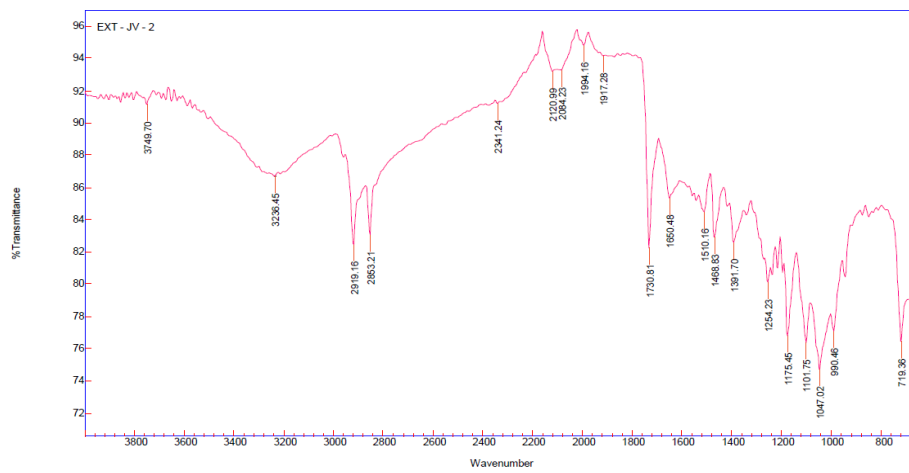


Figure S2. FTIR spectra of PLL-AuNPs.

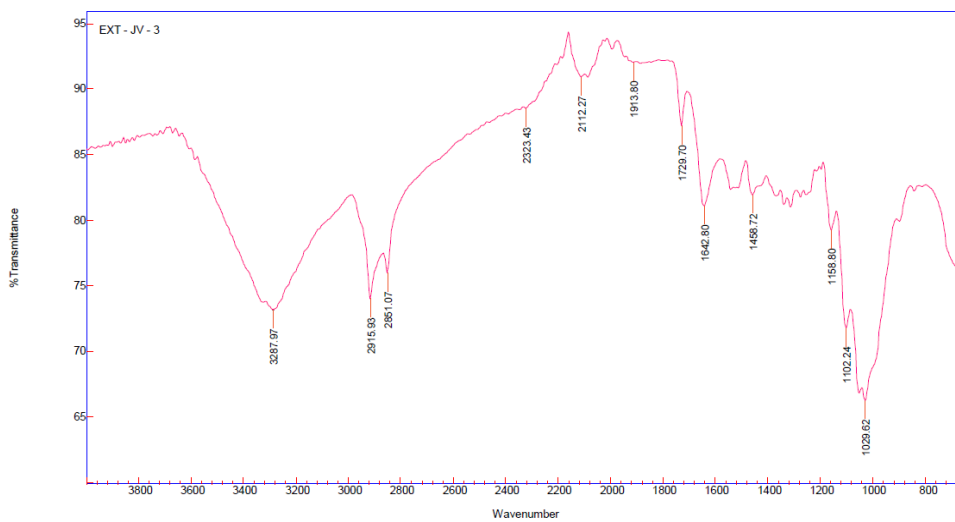


Figure S3. FTIR spectra of PEG-PLL-AuNPs.